Progress In Electromagnetics Research M, Vol. 74, 11–23, 2018

Thermal Characteristics of Switched Reluctance Motor under Different Working Conditions

Yukun Sun[1, 2], Binbin Zhang[1], Ye Yuan[1, *], and Fan Yang[1]

Abstract—Accurate analysis of the thermal field in switched reluctance motor (SRM) is critical to the service life and safety performance of the SRM. According to the general structure of SRM, a two-dimensional (2D) finite element analysis (FEA) model was established, and the loss of each component, especially the iron loss, was analyzed by Orthogonal Fourier decomposition method, revealing the characteristics of the loss. A magnetic-thermal one-way coupling method is further used to model the temperature of the SRM, and basic assumptions and reasonable boundary conditions are set. Transient thermal analysis was carried out under natural cooling conditions and high vacuum conditions, respectively, and the results were compared and analyzed to understand the temperature distribution of the main components under two operating conditions.

1. INTRODUCTION

Switched reluctance motor (SRM) is a doubly salient, single excited motor. It is constructed from a stack of salient-pole laminations, and only the stator carries the windings, which has many advantages such as simple structure, large mechanical strength, good speed regulation performance, low manufacturing cost, high reliability, flexible control mode, good fault tolerance and high efficiency. It is suitable for extreme environments such as high temperature and aerospace [1]. The use rate of SRM in various fields is increasing year by year, and it must be noticed that various machine parameters and designs in different running conditions are important factors which affect efficiency too. Designs of SRM with high torque, small size and that can work in low speed were developed. The motors designed here are suggested as an alternative to be used in mechanical systems without reductor [2, 3]. External rotor machines are typically more challenging to cool, and SRM also has different cooling requirements compared to permanent magnet machines [4, 5].

Due to good characteristics of SRM, it is often used in special operating condition; correspondingly, it is particularly important to analyze the temperature characteristics of the motor in different environments. However, it is worth noting that there are currently few studies on loss calculation and temperature analysis for SRM. With the rapid development of finite element software and the continuous verification of empirical formulas, the calculation of heat dissipation coefficient and thermal resistance can approximate the temperature distribution of the motor, but most of the researches are still in stage of simulation, and the heat transfer theory has not been studied in depth. In [6], the iron loss characteristics of SRM were studied, and the Stanmeet method was used to study the iron loss. Finally, the main parameters affecting the iron loss of the motor were analyzed. Ref. [7] introduced the motor optimization design based on the magneto-thermal coupling method. Ref. [8] proposed a fast and accurate analysis method to analyze the loss and efficiency of four-phase 16/12-pole SRM under

Received 13 July 2018, Accepted 16 September 2018, Scheduled 2 October 2018

* Corresponding author: Ye Yuan (1000050003@ujs.edu.cn).

[1] School of Electrical and Information Engineering, Jiangsu University, Zhenjiang 212013, China. [2] School of Power Engineering, Nanjing Institute of Technology, Nanjing 211167, China.

different working conditions. Ref. [9] proposed a calculation method for the copper loss of SRM high-efficiency windings, which has obvious advantages in optimizing the winding configuration. Refs. [10–12] analyzed the temperature rise caused by iron loss and copper loss in SRM by two-dimensional and three-dimensional finite element method. The analysis considers the effects of forced heat transfer and internal air temperature rise. Therefore, the temperature rise of the internal air increases the accuracy of the temperature calculation. Refs. [13–15] introduced the thermal modeling and analysis of the dual stator SRM and verified it through experiments. Refs. [16–19] introduced the temperature distribution of the motor under different conditions. However, the radiation heat dissipation is a nonlinear problem, and the finite element model is quite complicated to build. How to get an accurate convergence solution is a difficult point.

In this paper, a general 12/8 SRM 2D model is built, and the external circuit is used to supply. The total loss of the motor is revealed, and the iron loss of the motor is analyzed by the orthogonal Fourier decomposition method. The distribution characteristics of the losses are expounded. The magnetic-thermal unidirectional coupling method is used to build the temperature model of SRM, that is a 3D FEA model, and the basic assumptions and reasonable boundary conditions are given for the SMR's doubly salient structure and the special environment applied. Using these results as the heat source, the temperature is estimated. Transient thermal analysis was carried out under natural cooling conditions and high vacuum conditions, and the results were compared and analyzed to understand the temperature distribution of each component, which is the temperature of SRM under the corresponding working conditions. The reference is provided for temperature estimation, reliability analysis and electromagnetic design of SRM under corresponding working condition, which gives high requirements for the heat dissipation performance of the motor in the extreme environment and the importance of designing the cooling method. The outline of this analysis is indicated in Fig. 1.

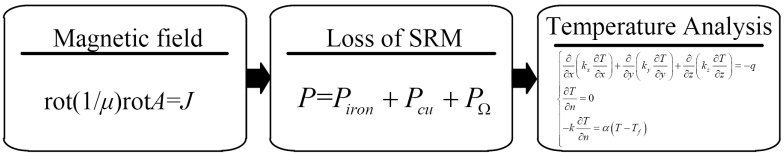

Figure 1. Outline of the temperature analysis.

2. SRM LOSS CHARACTERISTICS

The temperature field must be loaded with a heat source, and the heat source is mainly the loss of each part of the motor, so the accurate calculation of the loss is the premise of calculating the temperature field. The SRM motor used in this paper is a 12/8 SRM that is powered by an external circuit. The main parameters of the motor are shown in Table 1.

When the SRM works under different working conditions and does not consider the friction loss, the total loss is given as in Equation (1):

$$P = P_{iron} + P_{cu} + P_{\Omega} \tag{1}$$

where P — total loss; P_{iron} — core loss; P_{cu} — copper loss; P_{Ω} — additional loss. Copper loss can be calculated by Equation (2):

$$P_{cu} = qI^2R \tag{2}$$

where q — phase number; I — phase current; R — resistance of one phase.

The motor is a double salient pole structure, and the magnetic field changes on the stator and rotor are complicated; therefore, it is not a simple alternating magnetization and also a rotating magnetization. The traditional Bertotti iron loss model solution needs to obtain the loss coefficient of each part; however, it is not easy to calculate in practical applications. Different magnetic density distribution characteristics at different positions have a great influence on accurate analysis and calculation of stator core loss. The orthogonal Fourier decomposition method is used to analyze the core loss of the motor. The process is to decompose the magnetic density into a radial magnetic density

Table 1. Dimensions of SRM.

Parameter	Initial value	Parameter	Initial value
Rated power P/W	2200	Rotor outer diameter D_r/mm	70
Rated speed n/rpm	4000	Rotor inner diameter D_i/mm	31.5
Rated efficiency/η	0.80	Air gap g/mm	0.3
Rated voltage U/V	380	Axial length L/mm	68
Stator outer diameter D_s/mm	121	Pole arc $\beta/(^\circ)$	15

component and a tangential magnetic density component, perform alternating magnetization in two directions, and then perform the directions in each direction. The core loss is solved, and finally all the values are added to obtain the iron loss under the rotating magnetization. One of the split unit losses is shown in Equation (3) [8]:

$$\begin{aligned} P_{iron} &= \sum_{i=1}^{n} \left(k_h f_{ir} B_{irm}^{\alpha} + k_c f_{ir}^2 B_{irm}^2 + k_e f_{ir}^{1.5} B_{irm}^{1.5}\right) \\ &\quad + \sum_{j=1}^{n} \left(k_h f_{it} B_{jtm}^{\alpha} + k_c f_{jt}^2 B_{jtm}^2 + k_e f_{jt}^{1.5} B_{jtm}^{1.5}\right) \end{aligned} \tag{3}$$

where f_{ir} — frequency of flux density waveform of radial component at the i time (Hz);
f_{jt} — frequency of flux density waveform of tangential component at the i time (Hz);
B_{irm} — amplitude of flux density waveform of Radial component at the i time (T);
B_{jtm} — amplitude of flux density waveform of tangential component at the i time (T).

It can be seen from Equation (3) that the core loss and magnetic density amplitude are related to the harmonic frequency and loss factor. In order to accurately analyze the magnetic density characteristics of different positions of the stator and rotor, the stator and rotor are divided into five regions, respectively for tooth, tooth yoke junction and yoke. Select five nodes 1, 2, 3, 4 and 5 in five areas, and the distribution of each node is shown in Fig. 2.

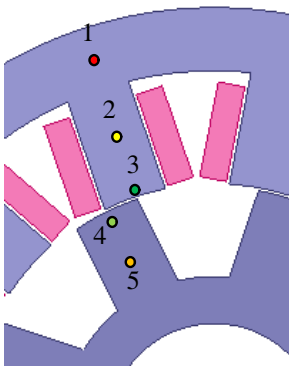

Figure 2. Location for the analysis of flux density.

It can be seen from Fig. 3 that flux density has been greatly changed in the radial magnetic density component Br and the tangential magnetic density component Bt at different positions of the stator and rotor. Point 1 contains both the component Br and component Bt, and Br is larger than Bt; the component Bt at point 2 is almost negligible which can be regarded as containing only the component Br; Point 3 contains both the component Br and component Bt, and the Br value is twice of the Bt value; the component Br at point 4 is substantially the same as the component Bt; the component Bt at 5 points is almost negligible. From the above analysis, it can be seen that, for SRM, the change of the

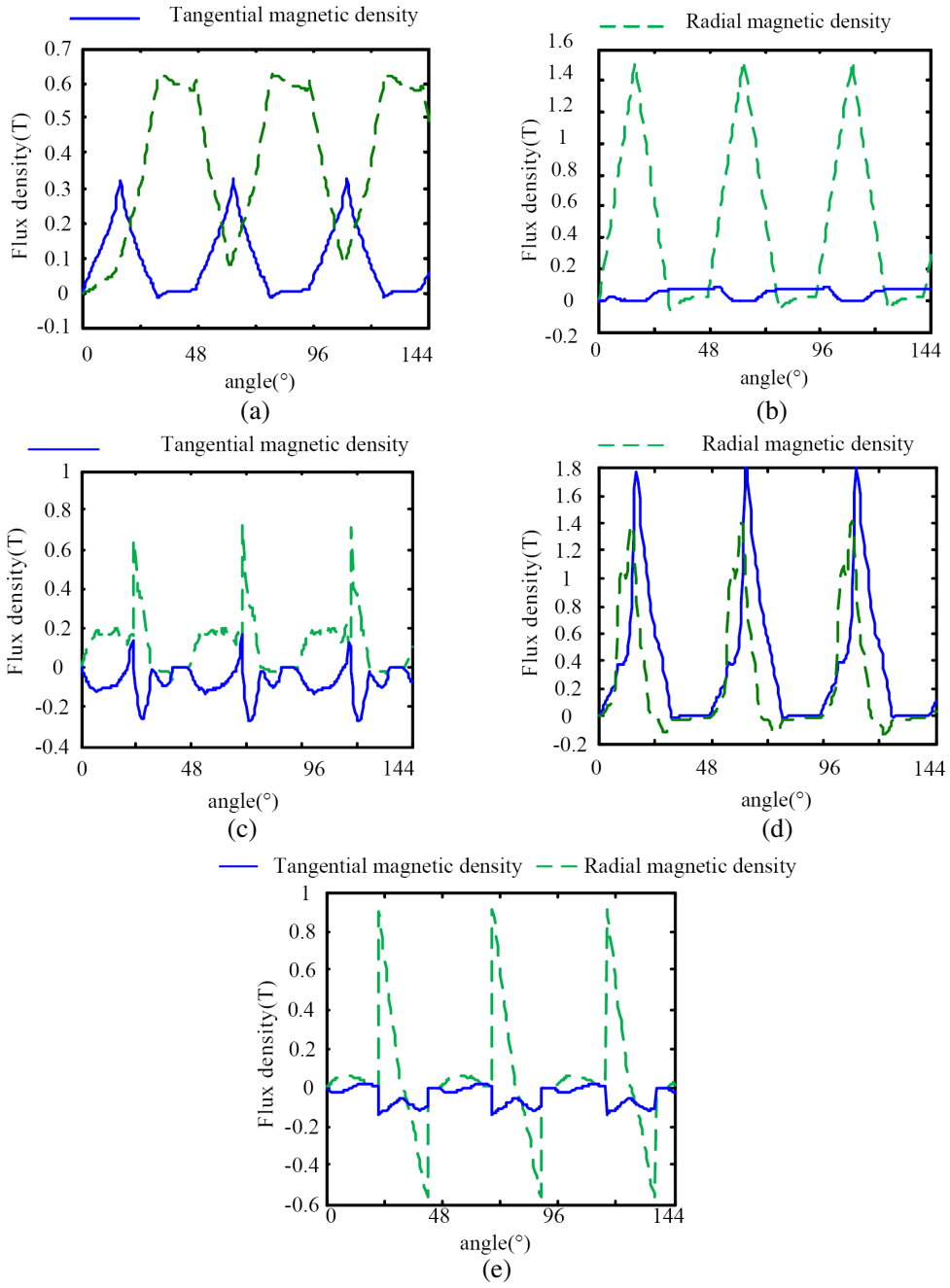

Figure 3. Flux density wave of different points in radial and tangential subspaces. (a) point 1, (b) point 2, (c) point 3, (d) point 4, (e) point 5.

magnetic density of the rotor core is more complicated than that of the stator core, and the harmonic content is large, but the magnetic density is obviously smaller [20]. The reason for the difference of magnetic flux density is that the magnetic field of switched reluctance motor is highly nonlinear. The waveform of each unit's section is different, and the magnitude of the flux density is also not the same. The core loss of SRM misaligned position is obtained by the finite element simulation, shown in Fig. 4. The core loss is mainly distributed in the stator and rotor tooth, and the loss of yoke is small, which verifies the above analysis.

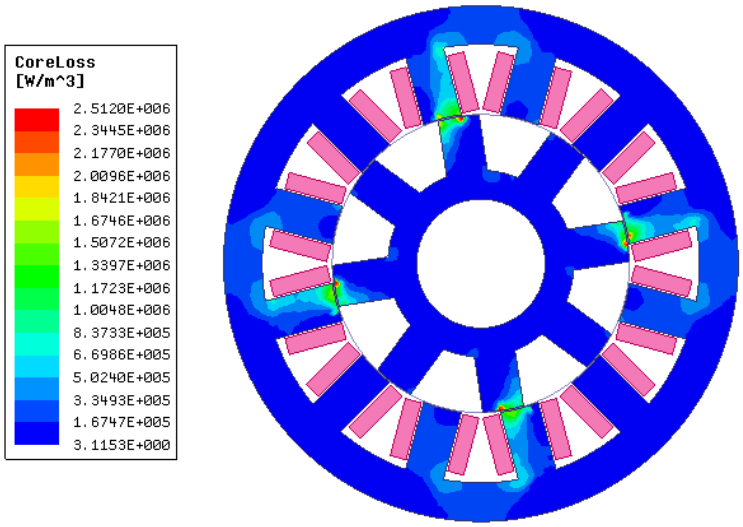

Figure 4. Core loss distribution of SRM.

3. THERMAL MODEL OF SRM

In this paper, the unidirectional coupling method is adopted, and the influence of temperature change on the motor parameters is not considered. The main analysis process is to determine the initial structural parameters of the SRM based on the motor design criteria. 2D models and 3D thermal analysis models were built using Ansys finite element analysis software. The electromagnetic performance of motor is analyzed in the solver to obtain the loss distribution of motor. Then the loss is introduced into the workbench 3D thermal model as a heat source for transient thermal analysis to obtain the temperature distribution of each component of the motor. Since the gas flow and heat transfer in the motor is a complicated process, in order to simplify the model, the following reasonable assumptions are given:

1) The thermal coefficients of the material do not change with temperature, and only the average effect of temperature is considered.
2) The ambient temperature of the motor remains unchanged, and the initial temperature of the motor is the same as the ambient temperature;
3) The heat dissipation coefficient is average value;
4) The motor adopts distributed winding, and the winding is replaced by a rectangular parallelepiped. All the insulation in the stator slot is insulated from the slot, and the winding copper wire is equivalent to a heat conductor;
5) Use the thermal conductivity of the stationary gas to equal the thermal conductivity of the air rotating in the air gap;
6) Ignoring the influence of the pole arc on the temperature distribution, the axial temperature gradient of the motor is considered to be zero.

Based on the above assumptions, when the motor is running transiently, the 3D heat conduction equation is as shown in Equation (4):

$$\begin{cases} \dfrac{\partial}{\partial x}\left(k_x \dfrac{\partial T}{\partial x}\right) + \dfrac{\partial}{\partial y}\left(k_y \dfrac{\partial T}{\partial y}\right) + \dfrac{\partial}{\partial z}\left(k_z \dfrac{\partial T}{\partial z}\right) = -q \\ \dfrac{\partial T}{\partial n} = 0 \\ -k\dfrac{\partial T}{\partial n} = \alpha\left(T - T_f\right) \end{cases} \tag{4}$$

where k_x, k_y, k_z — the thermal conductivity of the motor material in the x, y, and z directions; q — the sum of the density of each heat source; T — solution temperature of the object; α — heat dissipation coefficient of the surface; T_f — temperature of fluid around the heat surface.

The winding of the machine is a heterogeneous structure consisting of insulation, air and copper wires. These materials have totally different thermal behaviors. It is common practice to consider an equivalent thermal conductivity coefficient for the winding which can be obtained by various methods (analytical approach, FEM, experiments). In this model, conductors having the same temperature are lumped together to make a copper layer. Layers of copper that have roughly equal temperature are expected to have a similar distance from the stator laminations. The copper layer thickness is assumed equal to that of the bare conductor diameter, and the number of layers (with the spacing between them) is set so that the entire copper area is equal to that of the actual machine. This winding model helps to visualize the slot fill and show where the hot spot is likely to be.

Based on the above analysis, an equivalent 3D model is established as shown in Fig. 5. At the same time, the thermal conductivity of various components can be determined. Since the axial thermal conductivity of the copper strand and the stator core lamination is relatively high, and the radial difference is large. The material parameter is designed as shown in Table 2.

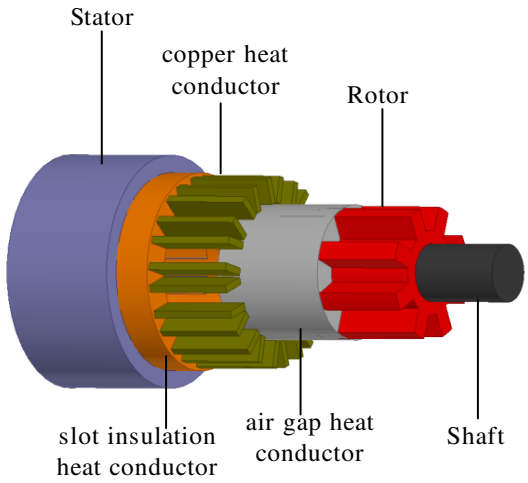

Figure 5. Temperature field model.

Table 2. Dimensions of material.

Part	material	density (kg/m^3)	Specific heat capacity (J/kg·K)	Thermal Conductivity (W/(m·K))
Stator and rotor	DW470	7800	450	70
slot insulation	Composite material	1.2	1340	0.3
Winding	Copper	8900	390	386
Air gap	Air	1.29	1004	0.023
Shaft	Aluminum	2700	903	204

4. SRM MAGNETIC-THERMAL COUPLING ANALYSIS

4.1. Temperature Analysis under Natural Cooling Conditions

The magneto-thermal finite element coupling simulation of the motor was carried out in ANSYS Workbench, and the loss of motor was introduced into the transient thermal analysis field as a heat

source. According to the heat transfer theory, in natural cooling condition, the heat conduction and heat convection between the components are the main heat dissipation methods, and the heat radiation can be neglected. The quality of heat conduction is mainly determined by the thermal conductivity of the material. The thermal convection is mainly determined by the surface heat dissipation coefficient of the component. The thermal conductivity of each component material can be set by Table 2. The difficulty is the surface heat dissipation coefficient of the component.

The stator and rotor are double salient pole structures. Therefore, the air gap between the stator and rotor changes constantly during rotating, and the heat dissipation process is complicated. It is difficult to establish an accurate model. Therefore, in order to simplify the calculation, the designer draws lessons from practice and uses the empirical formula to derive the convection coefficient over surface of each component under natural cooling conditions [6, 7].

1) Outer surface of stator yoke: It can be obtained by the empirical formula (5). When the external environment fluid of the motor does not flow, that is, $v = 0\,\mathrm{m/s}$, the heat dissipation coefficient $\alpha_1 = 14\,\mathrm{W/(mm^2 \cdot {}^\circ C)}$.

$$\alpha_1 = 14\left(1 + 0.5\sqrt{v}\right)^3 \sqrt{\frac{T_f}{25}} \tag{5}$$

2) Z face of Stator: It can be obtained by the empirical formula (6).

$$\alpha_2 = (1 + 0.04\omega)/0.045 \tag{6}$$

where, ω — linear velocity of rotor outer diameter.

3) Outer and inner face of rotor: Based on the previous assumptions, the heat dissipation coefficient is calculated by the following empirical formula.

$$\alpha_3 = Nu\lambda/g \tag{7}$$

$$Nu = 0.386Ta^{0.5}Pr^{0.27} \tag{8}$$

$$Ta = g\omega/u\sqrt{\frac{g}{R}} \tag{9}$$

$$Pr = u\rho C/\lambda \tag{10}$$

Where, Nu — Nusselt number; λ — thermal conductivity of Material; g — air gap; Ta — Taylor number; u — Viscosity coefficient; C — Specific heat capacity; Pr — Prandtl number.

4) Z face of rotor: It can be obtained by the empirical formula (11).

$$\alpha_4 = 28\left(1 + \sqrt{0.45v}\right) \tag{11}$$

The above boundary conditions are applied to the 3D thermal model to solve the problem, and the temperature distributions in stator and rotor are obtained as shown in Fig. 6. The temperature variation curve of each part of the motor is shown in Fig. 7.

As can be seen from Fig. 6, the temperature of stator is generally higher than the rotor side, because the core loss of stator is larger than the rotor. Moreover, the temperature is concentrated on the stator tooth, which is relatively larger than the stator yoke. Correspondingly, the temperature is also concentrated on the rotor tooth, which is relatively larger than the rotor yoke. The reason is that the rotor yoke is close to the external environment; the heat dissipation area is large; the heat dissipation condition is better. However, the pole teeth is very close to the air gap, and the heat dissipation condition is poor. It is basically consistent with the analysis of the first section of the electromagnetic loss.

Figure 7 shows the temperature variation curve of stator pole, rotor pole and winding. It can be seen that the temperature of motor rises faster in the first 30 minutes. The reason is that the initial temperature of motor is similar to the external ambient temperature; the heat generated by the loss is used to heat itself; the heat dissipation to the external environment is small. Within 30 to 60 minutes, the temperature of motor and the external environment are greatly different, and the motor temperature is slowly increased. The balance with the heat production is reached, and the temperature tends to reach a steady state, which basically does not change after 60 minutes. At this time, the temperature of

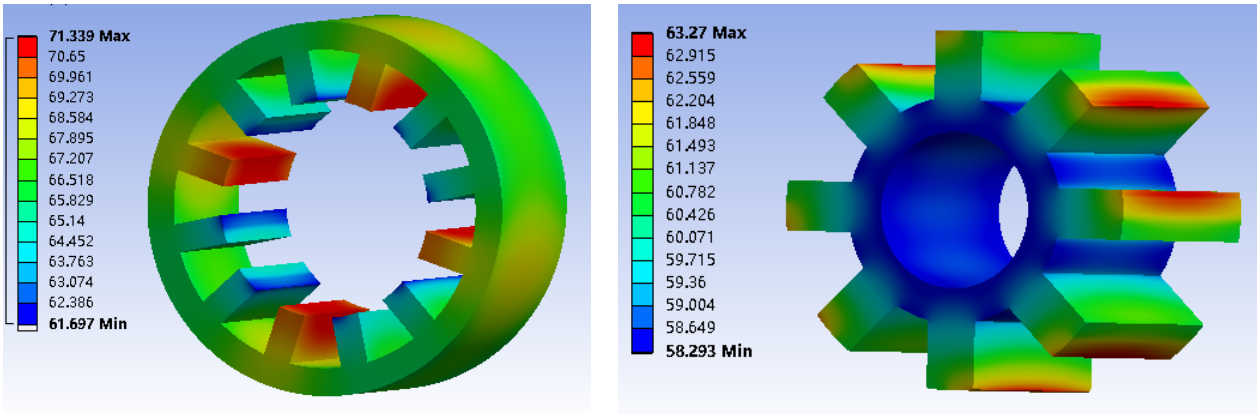

Figure 6. Temperature distribution in stator and rotor. (a) stator, (b) rotor.

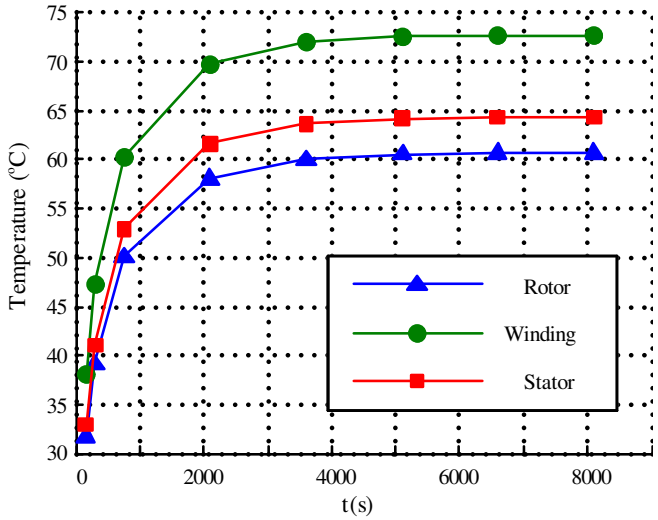

Figure 7. Temperature variation curve of each part of the motor.

stator pole tooth is about 65°C, the temperature of rotor pole tooth about 60°C, and the temperature of winding about 73°C. The average temperature relationship about the three is: winding > stator > rotor. The maximum temperature of simulation results appears in the internal coil, which is due to higher copper losses. Therefore, the coil winding itself is a powerful loss of heat source, and the insulation of winding and thermal conductivity of insulation medium are small. Meanwhile, cooling capacity is poor. There will be a greater impact on the spread of heat, and the two factors make the maximum temperature rise appear in the winding part. Therefore, the efficiency of heat conduction is higher than heat convection and heat radiation.

4.2. Temperature Analysis under High Vacuum Conditions

When the SRM works in a high vacuum environment, there is no medium. However, the convection and conduction both require medium to transfer heat, and the heat dissipation condition of the SRM is poor. Therefore, it is very important to analyze the heat dissipation of SRM in a vacuum environment. The formula for radiating heat between different objects is as follows:

$$Q_r = \sigma \gamma F_{ij} \left(T_1^4 - T_2^4\right) \tag{12}$$

Where, σ — Stefan-Boltzmann number; γ — The effective heating rate of the radiating surface which is related to the various coefficients of the material; T_1 — Temperature of the radiating surface 1; T_2 — Temperature of the radiating surface 2; F_{ij} — Radiation heat transfer angle coefficient.

It can be known from formula (12) that the amount of radiant heat dissipation between objects is determined by the angular coefficient, emissivity, and temperature of the heat dissipating object. The angle coefficient is solved as follows:

$$F_{ij} = \frac{F_j}{F_i} = \frac{1}{S_i} \int\limits_{S_i} \int\limits_{S_j} \frac{\cos\theta_i \cos\theta_j}{\pi r^2} dS_j dS_n \tag{13}$$

where S_i, S_j — Radiation heat dissipation area of different objects; r — Distance between radiating surfaces; θ_i, θ_j — The angle between the normal of the radiating surface and the two heat dissipating surfaces. The relationship is shown in Fig. 8.

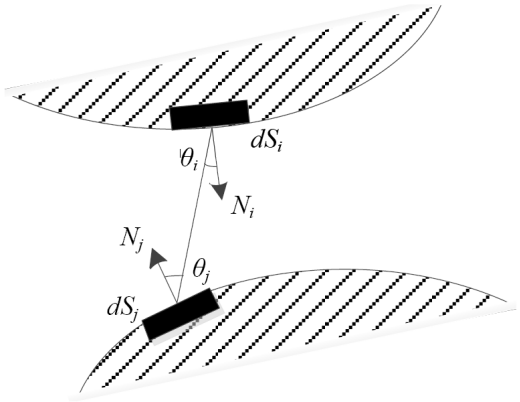

Figure 8. Angle location of radiating surface.

It can be known from Equation (13) that the angular coefficient is a dimensionless dimension, which is determined by the shape of the heat dissipating object. When the shape is constant, the angular coefficient is also determined. Therefore, the radiating heat depends largely on the emissivity.

Since the motor is operated under high vacuum conditions, the stator is mechanically connected to the vacuum chamber wall through the casing. It can be considered that the outer surface of the stator yoke is convectively dissipated with the external environment. The rotor is completely placed in the vacuum chamber, and there is no contact with the outside, so only radiation heat dissipation is considered. At this time, the heat dissipation environment of rotor is poor, and the temperature distribution should be analyzed. As shown in Fig. 9, the temperature distribution of rotor at different emissivity is revealed.

It can be seen from the cloud diagram that when the temperature reaches steady state, and the maximum temperature of the rotor is mainly concentrated on the middle part with the surface emissivity is 0.3, the surface emissivity is 0.9, and it has same situation. However, due to the isotropic nature of the materials, the temperature of each part of the rotor is relatively uniform, with little difference. The temperature variation curve of the rotor pole with different emissivity is shown in Fig. 10.

It can be seen from the variation curve that the temperature of rotor reaches a steady state in about 150 minutes. When the emissivity is 0.9, the temperature at which the rotor reaches a steady state is about 30°C lower than emissivity of 0.3. Surface emissivity has a great influence on the temperature distribution. The emissivity is proportional to the radiant heat dissipation. The larger the surface emissivity is, the more heat is radiated to the external environment.

The temperature distribution in stator and rotor with emissivity is 0.9 and under natural cooling is shown in Fig. 11. It can be seen that emissivity is 0.9, and the maximum temperature of the stator and rotor is still on the tooth pole, which is higher than stator yoke. However, the average temperature of rotor is higher than stator, because the stator yoke and vacuum chamber wall are connected, and

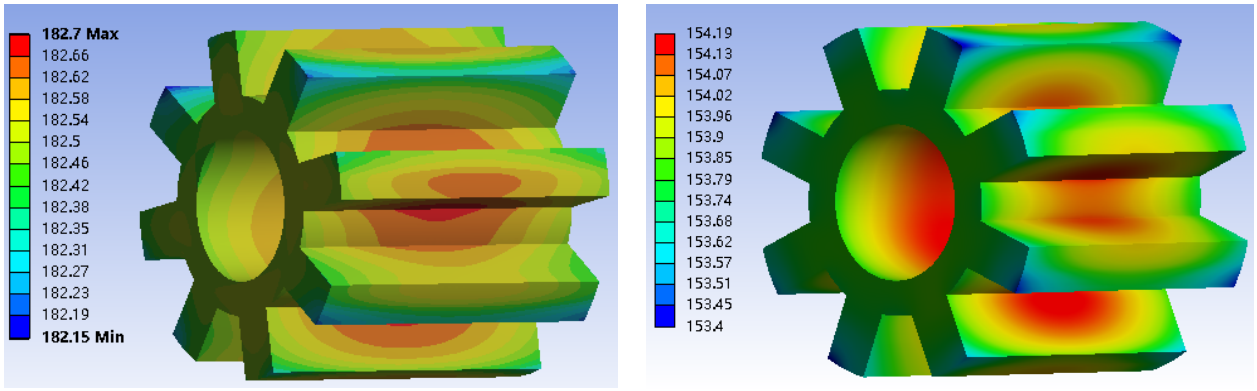

(a) (b)

Figure 9. Temperature distribution of different emissivity in rotor. (a) $\lambda = 0.3$, (b) $\lambda = 0.9$.

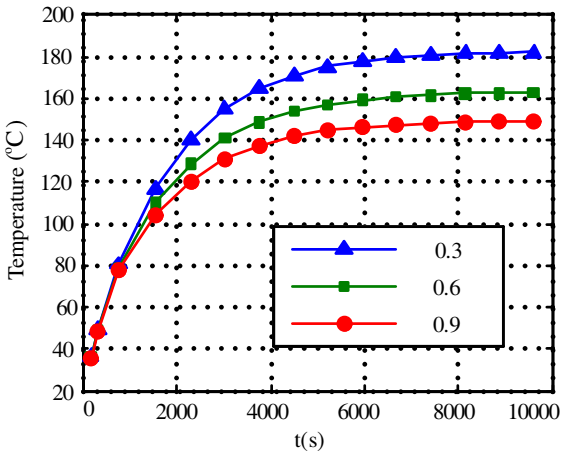

Figure 10. Temperature variation curve of different emissivity in rotor.

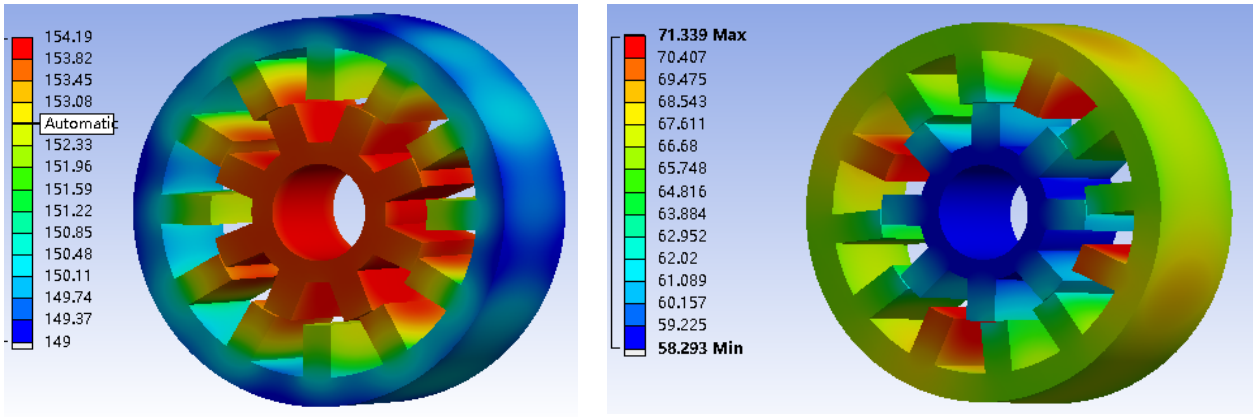

(a) (b)

Figure 11. Comparison of temperature distribution in stator and rotor under vacuum and natural working conditions. (a) $\lambda = 0.9$. (b) Natural cooling.

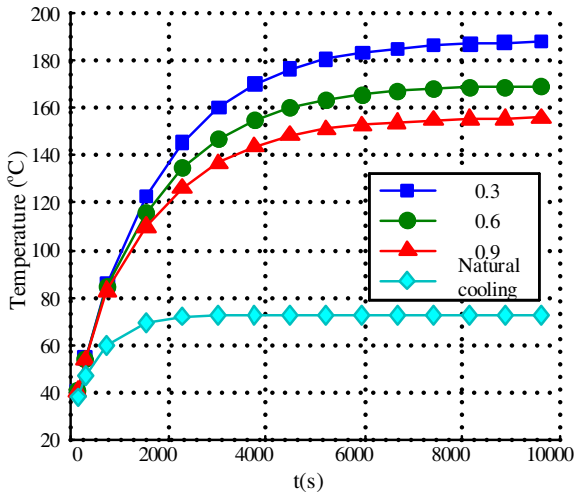

Figure 12. Temperature variation in winding under vacuum and natural working conditions.

then heat is dissipated by the heat convection with external air. Since there is no air between the stator and rotor, and the ambient temperature in the vacuum chamber is high, the rotor can only rely on radiation to dissipate heat; therefore, the rotor has strict heat dissipation conditions. Moreover, the minimum temperature of the rotor is higher than the maximum temperature of the stator. Conversely, the average temperature of the stator is higher than the rotor under natural cooling. At the same time, it can be found that even if the radiation emissivity is 0.9, the temperature of the motor is about twice as high as the temperature under natural cooling.

In order to observe the temperature changing under high vacuum environment more intuitively and clearly, the winding variation curve under two working conditions is shown in Fig. 12. From the variation curve, it is found that the temperature of winding decreases with the increase of the emissivity, and the steady-state temperature time is about 150 minutes; the steady-state temperature time is reached after about 60 minutes, and the heat of radiating is small, so the time to reach the steady state is longer. Therefore, heat dissipation of SRM in a high vacuum environment is difficult, and measures must be taken to improve the temperature level of the winding insulation and materials. At the same time, cooling measures must be designed to increase the radiation dissipation.

5. CONCLUSIONS

Aiming at the motor used in this paper and according to the simulation results of SRM temperature field, we can conclude that the iron loss is mainly distributed on the tooth of stator and rotor, and the iron loss of yoke is relatively small. Loss of motor is used as a heat source for subsequent temperature fields. Meanwhile, the simulation of the temperature distribution of SRM under different working conditions can be concluded:

1) In both cases, the temperature rises rapidly at the beginning, then slowly increases until the steady state is reached. The maximum temperature appears on the winding, and the temperature of tooth is higher than the yoke;
2) Under high vacuum conditions, the temperature of each component is about twice as high as that under natural cooling conditions, and the average temperature of rotor is higher than the stator.

In summary, various parts of SRM temperature distribution tendency are basically identical to the situation estimated in advance. It is shown that the established model and analysis method are basically correct and feasible. For other types of motors we can also use the same methods to deal with, and it has a certain guiding significance to verify whether the motor and its windings can work under rated conditions for long-term stability.

ACKNOWLEDGMENT

This work was sponsored by the National Natural Science Foundation of China (51707082, 51877101), Natural Science Foundation of Jiangsu Province (BK20170546), China postdoctoral science foundation (2017M620192) and Priority Academic Program Development of Jiangsu Higher Education Institutions.

REFERENCES

1. Liaw, C. M., K. W. Hu, J. C. Wang, et al., "Development and operation control of a switched-reluctance motor driven flywheel," *IEEE Transactions on Power Electronics*, Vol. PP, No. 99, 1-1, 2018.
2. Tarımer, İ and R. Gurbuz, "Sizing of electrical motors for gearless and directly stimulating applications," *Electronics & Electrical Engineering*, No. 4, 21–26, 2015.
3. Tarımer, İ, "Investigation of the effects of rotor pole geometry and permanent magnet to line start permanent magnet synchronous motor's efficiency," *Elektronika Ir Elektrotechnika*, No. 2, 67–72, 2009.
4. Inamura, S., T. Sakai, and K. Sawa, "A temperature rise analysis of switched reluctance motor due to the core and copper loss by FEM," *IEEE Transactions on Magnetics*, Vol. 39, No. 3, 1554–1557, 2003.
5. Castano, S. M., B. Bilgin, J. Lin, et al., "Radial forces and vibration analysis in an external-rotor switched reluctance machine," *IET Electric Power Applications*, Vol. 11, No. 2, 252–259, 2017.
6. Chen, H., Y. Xu, and H. C. Iu, "Analysis of temperature distribution in power converter for switched reluctance motor drive," *IEEE Transactions on Magnetics*, Vol. 48, No. 2, 991–994, 2012.
7. Sun, H., J. Gao, Y. Dong, et al., "Analysis of temperature field in switched reluctance motor based on finite-element," *Proceedings of the 11th International Conference on Electrical Machines and Systems*, Vol. 2, 597–601, 2008.
8. Boivie, J., "Iron loss model and measurements of the losses in a switched reluctance motor," *Sixth International Conference on Electrical Machines and Drives, IET*, 219–222, 1993.
9. Liu, C., X. Zhu, Y. Du, et al., "Design and performance analysis of magnetic field modulated flux-switching permanent magnet machine based on electrical-thermal bi-directional coupling design method," *Proceedings of the CSEE*, Vol. 37, No. 21, 6237–6245, 2017.
10. Yu, Q., B. Bilgin, and A. Emadi, "Loss and efficiency analysis of switched reluctance machines using a new calculation method," *IEEE Transactions on Industrial Electronics*, Vol. 62, No. 5, 3072–3080, 2015.
11. Yang, Y., B. Bilgin, M. Kasprzak, et al., "Thermal management of electric machines," *IET Electrical Systems in Transportation*, Vol. 7, No. 2, 104–116, 2016.
12. Eit, M. A., P. Dular, F. Bouillault, et al., "Perturbation finite element method for efficient copper losses calculation in switched reluctance machines," *IEEE Transactions on Magnetics*, Vol. 53, No. 6, 1–4, 2017.
13. Li, G. J., J. Ojeda, E. Hoang, et al., "Comparative studies between classical and mutually coupled switched reluctance motors using thermal-electromagnetic analysis for driving cycles," *IEEE Transactions on Magnetics*, Vol. 47, No. 4, 839–847, 2011.
14. Arbab, N., W. Wang, C. Lin, et al., "Thermal modeling and analysis of a double-stator switched reluctance motor," *IEEE Transactions on Energy Conversion*, Vol. 30, No. 3, 1209–1217, 2015.
15. Udhav, U. G., B. Ashok, D. Eshan, et al., "Thermal and mechanical design considerations for a switched reluctance motor," *2016 7th India International Conference on Power Electronics (IICPE), IEEE*, 1–6, 2016.
16. Howey, B., E. Rowan, B. Bilgin, et al., "Thermal trade-off analysis of an exterior rotor e-bike switched reluctance motor," *IEEE Transportation Electrification Conference and Expo (ITEC)*, 605–612, 2017.
17. Jang, J. H., H. C. Chiu, W. M. Yan, et al., "Numerical study on electromagnetics and thermal cooling of a switched reluctance motor," *Case Studies in Thermal Engineering*, Vol. 6: 16–27, 2015.

18. Kasprzak, M., J. W. Jiang, B. Bilgin, et al., "Thermal analysis of a three-phase 24/16 switched reluctance machine used in HEVs," *IEEE Energy Conversion Congress and Exposition (ECCE)*, 1–7, 2016.
19. Raminosoa, T., B. Blunier, D. Fodorean, et al., "Design and optimization of a switched reluctance motor driving a compressor for a PEM fuel-cell system for automotive applications," *IEEE Transactions on Industrial Electronics*, Vol. 57, No. 9, 2988–2997, 2010.
20. Huang, X. and X. Wang, "Switched reluctance motor loss optimization based on finite element method," *2016 International Symposium on Computer, Consumer and Control (IS3C)*, 567–570, 2016.